



Cite as  
Nano-Micro Lett.  
(2019) 11:65

Received: 5 June 2019  
Accepted: 16 July 2019  
Published online: 2 August 2019  
© The Author(s) 2019

## Electrostatic Self-assembly of 0D–2D SnO<sub>2</sub> Quantum Dots/Ti<sub>3</sub>C<sub>2</sub>T<sub>x</sub> MXene Hybrids as Anode for Lithium-Ion Batteries

Huan Liu<sup>1</sup>, Xin Zhang<sup>2</sup>, Yifan Zhu<sup>2</sup>, Bin Cao<sup>2</sup>, Qizhen Zhu<sup>2</sup>, Peng Zhang<sup>2</sup>, Bin Xu<sup>2</sup> ✉, Feng Wu<sup>1</sup>, Renjie Chen<sup>1</sup> ✉

Huan Liu and Xin Zhang have contributed equally to this work.

✉ Bin Xu, [binxumail@163.com](mailto:binxumail@163.com); Renjie Chen, [chenrj@bit.edu.cn](mailto:chenrj@bit.edu.cn)

<sup>1</sup> School of Materials Science and Engineering, Beijing Key Laboratory of Environmental Science and Engineering, Beijing Institute of Technology, Beijing 100081, People's Republic of China

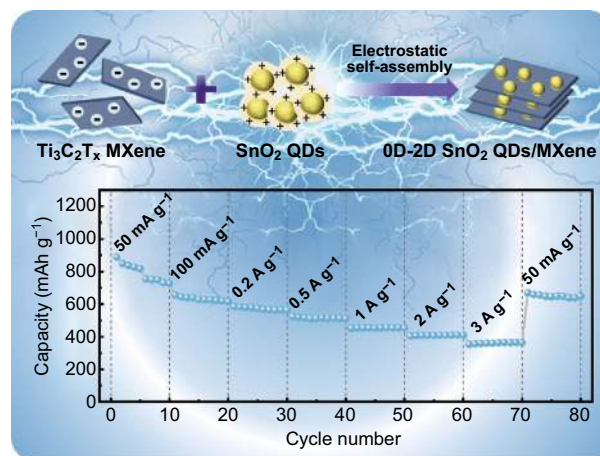
<sup>2</sup> State Key Laboratory of Organic-Inorganic Composites, Beijing Key Laboratory of Electrochemical Process and Technology for Materials, Beijing University of Chemical Technology, Beijing 100029, People's Republic of China

### HIGHLIGHTS

- 0D–2D SnO<sub>2</sub> quantum dots/MXene (SnO<sub>2</sub> QDs/MXene) hybrids were synthesized by electrostatic self-assembly.
- MXene not only provides efficient pathways for fast transport of electrons and Li ions, but also buffers the volume change of SnO<sub>2</sub> during charge/discharge process.
- The 0D–2D SnO<sub>2</sub> QDs/MXene hybrids deliver high capacity, excellent cycle and rate performances as anode of lithium-ion batteries.

**ABSTRACT** MXenes, a new family of two-dimensional (2D) materials with excellent electronic conductivity and hydrophilicity, have shown distinctive advantages as a highly conductive matrix material for lithium-ion battery anodes. Herein, a facile electrostatic self-assembly of SnO<sub>2</sub> quantum dots (QDs) on Ti<sub>3</sub>C<sub>2</sub>T<sub>x</sub> MXene sheets is proposed. The as-prepared SnO<sub>2</sub>/MXene hybrids have a unique 0D–2D structure, in which the 0D SnO<sub>2</sub> QDs (~4.7 nm) are uniformly distributed over 2D Ti<sub>3</sub>C<sub>2</sub>T<sub>x</sub> MXene sheets with controllable loading amount. The SnO<sub>2</sub> QDs serve as a high capacity provider and the “spacer” to prevent the MXene sheets from restacking; the highly conductive Ti<sub>3</sub>C<sub>2</sub>T<sub>x</sub> MXene can not only provide efficient pathways for fast transport of electrons and Li ions, but also buffer the volume change of SnO<sub>2</sub> during lithiation/delithiation by confining SnO<sub>2</sub> QDs between the MXene nanosheets. Therefore, the 0D–2D SnO<sub>2</sub> QDs/MXene hybrids deliver superior lithium storage properties with high capacity (887.4 mAh g<sup>-1</sup> at 50 mA g<sup>-1</sup>), stable cycle performance (659.8 mAh g<sup>-1</sup> at 100 mA g<sup>-1</sup> after 100 cycles with a capacity retention of 91%) and excellent rate performance (364 mAh g<sup>-1</sup> at 3 A g<sup>-1</sup>), making it a promising anode material for lithium-ion batteries.

**KEYWORDS** MXene; SnO<sub>2</sub>; Quantum dots; 0D–2D hybrid; Lithium-ion battery



Therefore, the 0D–2D SnO<sub>2</sub> QDs/MXene hybrids deliver superior lithium storage properties with high capacity (887.4 mAh g<sup>-1</sup> at 50 mA g<sup>-1</sup>), stable cycle performance (659.8 mAh g<sup>-1</sup> at 100 mA g<sup>-1</sup> after 100 cycles with a capacity retention of 91%) and excellent rate performance (364 mAh g<sup>-1</sup> at 3 A g<sup>-1</sup>), making it a promising anode material for lithium-ion batteries.

## 1 Introduction

Lithium-ion batteries (LIBs) are widely used in various portable electronics, electric tools, and electric vehicles due to their high energy density, long cycle life, and environmental friendly [1, 2]. Nevertheless, the conventional graphite anode of LIBs with a specific capacity of 372 mAh g<sup>-1</sup> can hardly meet the rapidly increasing demand of high energy density. Great efforts have been made to develop promising anode materials with high capacity, such as transition metal oxides [3, 4], alloys [5, 6], metal oxides/sulfates [7–9], and phosphorous [10–12]. Among various metal oxides, SnO<sub>2</sub> has attracted a lot of attention due to its relatively high theoretical capacity (790 mAh g<sup>-1</sup>, which is twice than the currently used graphite), low average working potential (~0.6 V vs. Li<sup>+</sup>/Li), natural abundance and low price [13–16]. Unfortunately, its practical application as anode material in LIBs is seriously limited by the poor cycle stability resulting from the severe volume change (> 300 vol%) during the charge/discharge process. Meanwhile, SnO<sub>2</sub> also suffers from low electrical conductivity, resulting in poor rate capability. To improve the electrochemical performances of SnO<sub>2</sub>, several strategies have been proposed to overcome these issues. One of the effective way is to fabricate nanostructured SnO<sub>2</sub>, such as SnO<sub>2</sub> quantum dots (QDs) [17], SnO<sub>2</sub> hollow spheres [18], or SnO<sub>2</sub> nanowires [19], which could restrain the structure changes during lithium alloying and shorten the ion diffusion lengths [20]. The other way is to combine SnO<sub>2</sub> with various carbon materials possessing high conductivity such as carbon nanotubes, carbon fiber or graphene [21–26]. The conductive carbon can not only improve the overall electrical conductivity of the composites but also act as a buffer to slow down the structure collapse of the electrode.

MXenes are a newly emerging family of 2D materials with a general formula of M<sub>n+1</sub>X<sub>n</sub>T<sub>x</sub>, where *M* represents early transition metal (*M* = Ti, Sr, V, Cr, Ta, Nb, Zr, Mo, and Hf), *X* is carbon and/or nitrogen, and *T* stands for the surface termination groups (–OH, –F=O) [27–31]. Due to their excellent electrical conductivity, tailorable surface chemistries, and mechanical properties, MXenes have recently attracted great interests in energy storage devices such as LIBs, sodium-ion batteries, and supercapacitors [32–35]. Particularly, as one of the most widely studied MXenes, Ti<sub>3</sub>C<sub>2</sub>T<sub>x</sub> is a potential anode material for LIBs, which can deliver excellent cycle stability and superior rate

performances. However, the theoretical reversible capacity of Ti<sub>3</sub>C<sub>2</sub>T<sub>x</sub> is only 320 mAh g<sup>-1</sup> [36]. On the other hand, MXene can also be used as a substrate to fabricate hybrids with other active materials, including metal oxides, which have higher theoretical capacity but poor conductivity and are prone to large volume change during charge/discharge. In the hybrids, MXene can improve the conductivity and buffer the volume changes of the metal oxide, while the metal oxide provides high capacity. Thus, the MXene/metal oxide hybrid could achieve high capacity, stable cycle and good rate performance [37–41]. For example, Ti<sub>3</sub>C<sub>2</sub>T<sub>x</sub>/Fe<sub>2</sub>O<sub>3</sub> nanocomposite was prepared by confining Fe<sub>2</sub>O<sub>3</sub> nanoparticles into Ti<sub>3</sub>C<sub>2</sub>T<sub>x</sub> nanosheets through ball-milling method, which showed reversible capacities of ~203 mAh g<sup>-1</sup> at 1 C and 100 mAh g<sup>-1</sup> at 10 C [37]. MXene/NiCo<sub>2</sub>O<sub>4</sub> composite with a capacity reaching up to 1330 mAh g<sup>-1</sup> was synthesized by spray coating method [38]. Some recent works indicate that MXene is also a good substrate to improve the lithium storage performance of SnO<sub>2</sub>. The hybrids of SnO<sub>2</sub> with MXene prepared by wet hydrothermal approach has shown a high capacity of 1021 mAh g<sup>-1</sup> and improved cycle stability [40]. However, a few reports indicate that MXene is unavoidable to be oxidized to titanium dioxide (TiO<sub>2</sub>) as a by-product during these processes, thereby, influencing the electrochemical performance of the composites. Recently, our group proposed a general route to self-assemble transition metal oxide nanostructures on Ti<sub>3</sub>C<sub>2</sub>T<sub>x</sub> MXene nanosheets through van der Waals interaction. The proposed method allowed fabrication of hybrids without getting MXene to be oxidized and achieved enhanced cycle and rate performance [15].

In this work, a simple method is proposed to prepare 0D–2D SnO<sub>2</sub> QDs/MXene hybrids by electrostatic self-assembling SnO<sub>2</sub> QDs on the surface of 2D Ti<sub>3</sub>C<sub>2</sub>T<sub>x</sub> MXene nanosheets under ultrasonication. Since, the synthesis is accomplished in a very mild condition, i.e., ultrasonication treatment of the mixture of negatively charged MXene and positively charged SnO<sub>2</sub> QDs at room temperature, the MXene oxidation is effectively avoided. In the hybrids, 2D nanosheet of MXene acts as a substrate to support 0D SnO<sub>2</sub> QDs, which can not only provide large electrode/electrolyte interface area for fast reversible transport of electrons and ions, but could also inhibit the aggregation of SnO<sub>2</sub> QDs and buffer the volume changes during charge/discharge process. The SnO<sub>2</sub> QDs with ultra-small particle size can effectively maximize the activity and specific capacity and minimize

the volume change while inhibiting the structure collapse during charge/discharge process and shortening the lithium diffusion pathways. In addition, the SnO<sub>2</sub> QDs acts as a “spacer” to prevent the MXene nanosheets from restacking and thus protecting the Li<sup>+</sup> migration channels and active sites. These unique features endow the 0D–2D SnO<sub>2</sub> QDs/MXene hybrids with high lithium storage capacity, excellent cycle stability and superior rate performance, indicating a promising anode for LIBs.

## 2 Experimental

### 2.1 Synthesis of Ti<sub>3</sub>C<sub>2</sub>T<sub>x</sub> MXene

The Ti<sub>3</sub>C<sub>2</sub>T<sub>x</sub> MXene was synthesized by etching Ti<sub>3</sub>AlC<sub>2</sub> (400 mesh, purchased from Yiyi Technology Co., Ltd.) with LiF + HCl solution as reported previously [41]. Typically, 1.0 g Ti<sub>3</sub>AlC<sub>2</sub> powder was subjected to a mixture containing LiF (1.0 g) and hydrochloric acid (12 M, 10 mL) under stirring conditions for 24 h at 35 °C. After several times of centrifugation-washing with deionized (DI) water, the product was then dispersed in 50 mL DI water, stored under ultrasound for 30 min. The dark green supernatant was collected by centrifugation at 3500 rpm for 1 h. Finally, the black MXene liquid was obtained and sealed for future use.

### 2.2 Synthesis of SnO<sub>2</sub> QDs

In order to obtain SnO<sub>2</sub> QDs, 4 mmol SnCl<sub>2</sub>·2H<sub>2</sub>O and 4 mmol thiourea (CH<sub>4</sub>N<sub>2</sub>S) were added to 30 mL DI water and magnetically stirred at room temperature to form a milky suspension. After stirring for 24 h, a clear yellow aqueous solution containing SnO<sub>2</sub> QDs was obtained.

### 2.3 Synthesis of 0D–2D SnO<sub>2</sub> QDs/MXene Hybrids

In a typical synthesis, 5 mL of as-prepared SnO<sub>2</sub> QDs solution was added to 40 mg 0.1 mg mL<sup>-1</sup> Ti<sub>3</sub>C<sub>2</sub>T<sub>x</sub> MXene solution under ultrasonication for 6 h. The SnO<sub>2</sub> QDs were deposited on the Ti<sub>3</sub>C<sub>2</sub>T<sub>x</sub> layers during this process and solid–liquid separation was observed. Finally, the black precipitate of SnO<sub>2</sub> QDs/MXene hybrids were collected by vacuum filtration, washed with water and dried in a vacuum

oven at 80 °C for 6 h. The above hybrid was denoted as SnO<sub>2</sub> QDs/MXene-52. For comparison, we also prepared another SnO<sub>2</sub> QDs/Ti<sub>3</sub>C<sub>2</sub>T<sub>x</sub> hybrids (SnO<sub>2</sub> QDs/MXene-51) under the same conditions, but the addition amount of MXene in this solution was 20 mg.

### 2.4 Materials Characterization

Scanning electron microscopy (SEM) characterization was conducted using a Gemini SEM 500. Transmission electron microscopy (TEM) characterization was conducted on a JEOL JEM-F200 (HR) equipped with selected area electron diffraction (SAED). X-ray diffraction (XRD) patterns were recorded on a Bruker D8 ADVANCE with monochromatic Cu K $\alpha$  radiation ( $\lambda = 1.54060 \text{ \AA}$ ). Raman spectra were obtained with a LabRAM HR Evolution Raman spectrometer (633 nm). X-ray photoelectron spectroscopy (XPS) analysis was performed using a Thermo Fisher ESCALAB Xi<sup>+</sup> to analyze the chemical compositions of the samples.

### 2.5 Electrochemical Measurements

The working electrodes were prepared by mixing 80 wt% active material, 10 wt% Super P and 10 wt% carboxymethylated cellulose (CMC) in DI water. After coating the slurry on the copper foil, the electrodes were dried at 60 °C in vacuum oven for 8 h to remove the solvent. To test electrochemical performances, CR2025-type coin cells were assembled in an argon-filled glove box (Mikrouna, H<sub>2</sub>O, O<sub>2</sub> < 0.1 ppm) using Li foil as half-cell counter electrode, and microporous membrane (Celgard 2400) as separator. The electrolyte was 1 M LiPF<sub>6</sub> in a mixture of ethylene carbonate (EC)/diethyl carbonate (DEC)/dimethyl carbonate (DMC) with a volume ratio of 1:1:1. The charge/discharge (GCD) tests were performed using a LAND BT2000 battery tester. The potential window was 0.01–2.5 V versus Li/Li<sup>+</sup>. The CV traces were recorded on a CS350 electrochemical workstation from 0.01 to 2.5 V. Electrochemical impedance spectroscopy (EIS) measurements were performed on the VSP Bio-Logic SAS at frequencies ranging from 10 mHz to 100 kHz with an applied AC signal amplitude of 10 mV. The capacities of the samples were calculated based on all the components in the active materials, i.e., the mass of SnO<sub>2</sub> QDs/Ti<sub>3</sub>C<sub>2</sub>T<sub>x</sub> hybrids.



### 3 Results and Discussion

The synthesis route for 0D–2D SnO<sub>2</sub> QDs/MXene by electrostatic self-assembly is illustrated in Fig. 1. Firstly, transparent yellow aqueous solution of positively charged SnO<sub>2</sub> QDs is prepared by hydrolysis, dehydration and oxidation of SnCl<sub>2</sub>·2H<sub>2</sub>O in DI water, where thiourea is added as a promoter and stabilizer (Fig. S1a). The mercaptan group can easily bound to Sn<sup>2+</sup>, and the SnO<sub>2</sub> QDs whose zeta potential is +99.0 mV (Fig. S1b) is surrounded by a positively charged protic amino group (–NH<sub>3</sub><sup>+</sup>), which makes it highly stable and electropositive [42]. The Ti<sub>3</sub>C<sub>2</sub>T<sub>x</sub> MXene solution with its negatively charged groups (–F, –OH) [43], and zeta potential of –36.2 mV, is very stable in water (Fig. S1a) due to the hydrophilicity and electrostatic repulsion between neighboring nanosheets. When positively charged SnO<sub>2</sub> QDs are added into the negatively charged Ti<sub>3</sub>C<sub>2</sub>T<sub>x</sub> colloidal solution, the SnO<sub>2</sub> QDs can easily load onto the surface of the

MXene nanosheets. After the continuous ultrasonication of 6 h, the supernatant becomes clear and colorless, and black precipitates are obtained. The positively charged SnO<sub>2</sub> QDs are captured by the negatively charged MXene nanosheets only by ultrasonic treatment without other components and additional treatments, implying an electrostatic self-assembly mechanism for the designed 0D–2D SnO<sub>2</sub> QDs/MXene hybrids. The Ti<sub>3</sub>C<sub>2</sub>T<sub>x</sub> MXene with 2D layered structure as a conductive matrix facilitates the charge transfer and accommodates the volume change of SnO<sub>2</sub> QDs; the SnO<sub>2</sub> QDs thus prevents the MXene nanosheets from restacking by working as “spacer” and providing channels for fast transfer of Li ion with promising electrochemical performance.

SEM and TEM were employed to characterize the morphology and structure of the as-prepared samples. The pure Ti<sub>3</sub>C<sub>2</sub>T<sub>x</sub> (Fig. S1c) displays a compact 2D layered structure. After decoration with SnO<sub>2</sub> QDs, the SnO<sub>2</sub> QDs/MXene hybrids exhibit 0D–2D structure, as shown in Fig. 2a. From

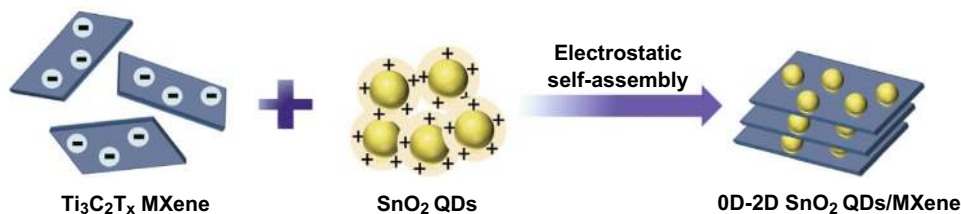


**Fig. 1** Schematic illustration for the preparation of 0D–2D SnO<sub>2</sub> QDs/MXene hybrids

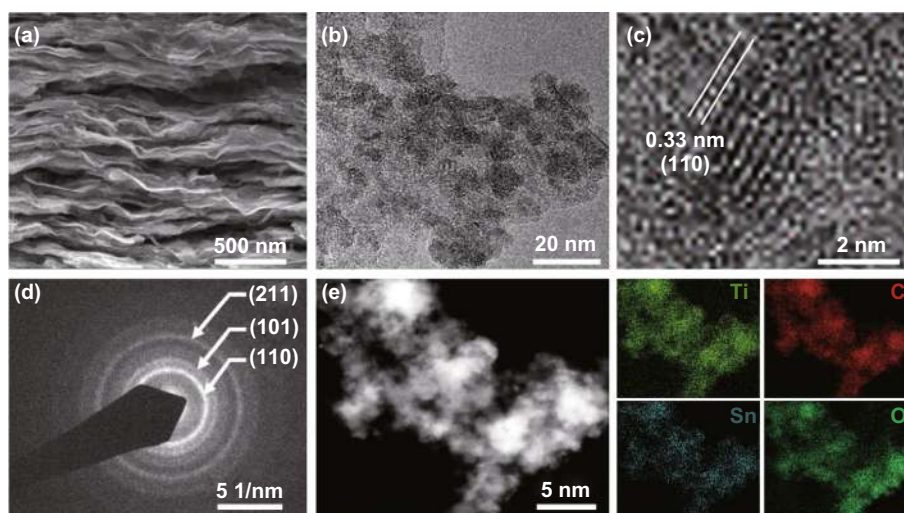


**Fig. 2** **a** SEM image, **b** TEM image, **c** HRTEM image of 0D–2D SnO<sub>2</sub> QDs/MXene hybrid. **d** SAED patterns of SnO<sub>2</sub> QDs. **e** STEM image and corresponding elemental mapping images of Ti, C, Sn, and O

a closer view in Fig. 2b, it can be seen that the spatially dispersed SnO<sub>2</sub> QDs are evenly distributed over the surface of the MXene nanosheets. The particle-size distribution analysis (Fig. S1d) indicates the SnO<sub>2</sub> QDs have an average particle size of ~4.5 nm, favoring the electrode/electrolyte interactions. Since the diffusion of Li ions is strongly dependent on the transport length and the active sites, the ultra-small particle size of SnO<sub>2</sub> QDs can not only expose a large number of electrochemical active sites shuttling Li ions in and out, but also shorten the diffusion path of Li ion transport, which are beneficial for improving the capacity and rate performance. Figure 2c shows clear lattice fringes of the SnO<sub>2</sub> QDs, indicating a high degree of crystallinity. The crystal lattice with a spacing of 0.33 nm is consistent with the d spacing of (110) planes of the SnO<sub>2</sub> tetragonal phase. The selected area electron diffraction (SAED) pattern (Fig. 2d) shows clear diffraction rings, implying the polycrystalline nature of SnO<sub>2</sub>. These diffraction rings can be well indexed to the (110), (101), and (211) planes of SnO<sub>2</sub>. Moreover, the typical scanning TEM (STEM) and elemental mapping images of SnO<sub>2</sub> QDs/MXene hybrid (Fig. 2e) show homogeneously distributed Ti, C, Sn, and O elements, demonstrating the uniform loading of SnO<sub>2</sub> QDs on the surface of MXene sheets.

The phase structures of the as-prepared SnO<sub>2</sub> QDs/MXene hybrids were verified by XRD as shown in Fig. 3a. Ti<sub>3</sub>C<sub>2</sub>T<sub>x</sub> exhibits the major peaks, such as the (002), (006), (008), (0010), and (0012) [44]. Typically, the (002) plane of the Ti<sub>3</sub>C<sub>2</sub>T<sub>x</sub> MXene is located at  $2\theta = 6.4^\circ$ , corresponding to an interplanar spacing of 13.7 Å [45]. In addition, the pure tetragonal phase of crystalline SnO<sub>2</sub> (JCPDS No. 41-1445) is located at  $26.5^\circ$ ,  $34.1^\circ$ , and  $52.4^\circ$ , corresponding to (110), (101), and (211). The XRD patterns of the SnO<sub>2</sub> QDs/MXene hybrids consist of Ti<sub>3</sub>C<sub>2</sub>T<sub>x</sub> and tetragonal phase SnO<sub>2</sub>, indicating that SnO<sub>2</sub> QDs/MXene hybrids have successfully formed. No any extra crystalline phase peaks such as TiO<sub>2</sub> are observed, indicating the electrostatic self-assembly process is mild with no oxidation of MXene. In addition, the (002) peak of the SnO<sub>2</sub>-MXene composite (Fig. S1e) was downshifted compared to pure MXene, indicating increased interlayer spacing of the MXene in the hybrids.

Raman spectra further confirm the phase characteristics of the SnO<sub>2</sub> QDs/MXene-52 hybrid. As shown in Figs. 3b and S1f, the peaks of pure SnO<sub>2</sub> at 271, 465, and 698 cm<sup>-1</sup> can be assigned to the E<sub>g</sub> and A<sub>1g</sub> active mode of SnO<sub>2</sub>, respectively [46]. Moreover, the pure MXene exhibits a peak at 199 cm<sup>-1</sup>

which corresponds to the A<sub>1g</sub> symmetry out-of-plane vibrations of Ti atoms, whereas the peaks at 381 and 622 cm<sup>-1</sup> are related to the E<sub>g</sub> group vibrations, including in-plane (shear) modes of Ti, C, and surface functional group atoms [47]. For the SnO<sub>2</sub> QDs/MXene-52, the spectrum manifests six cognizable Raman-active modes, combining the characteristic Raman peaks of Ti<sub>3</sub>C<sub>2</sub>T<sub>x</sub> and SnO<sub>2</sub>. In comparison with the pure SnO<sub>2</sub>, the peak intensity of SnO<sub>2</sub> in the hybrid has significantly declined. This suggests that the SnO<sub>2</sub> QDs are well separated by the Ti<sub>3</sub>C<sub>2</sub>T<sub>x</sub> nanosheets, which weakens the Raman signal from the SnO<sub>2</sub>. It's worth noting that no strong peak for TiO<sub>2</sub> was detected at 144 cm<sup>-1</sup>, confirming that MXene has not oxidized during the hybrid formation.

The elemental composition of SnO<sub>2</sub> QDs/MXene hybrid was further analyzed by XPS. For pristine Ti<sub>3</sub>C<sub>2</sub>T<sub>x</sub> MXene, there are only four main elements, Ti, C, F, and O, whereas for SnO<sub>2</sub> QDs/MXene-52, the Sn element is also detected, indicating the presence of SnO<sub>2</sub> in the hybrid (Fig. S2a). In the high-resolution C 1s spectrum (Fig. 3c), the characteristic peaks correspond to C-Ti (284.2 eV), C-C (288.7 eV), C-O (288.1 eV), C=O (289.5 eV), and O-C=O (291.6 eV) [48]. The particular peak located at 282.1 eV can be assigned to the C-Ti bond in Ti<sub>3</sub>C<sub>2</sub>T<sub>x</sub> sheets. The XPS spectrum of the Ti 2p (Fig. 3d) reveals that peaks of Ti bound to C, Ti(II), and Ti(III). The Ti-C 2p<sub>3/2</sub>, Ti(II) 2p<sub>3/2</sub>, Ti(III) 2p<sub>3/2</sub>, Ti-C 2p<sub>1/2</sub>, Ti(II) 2p<sub>1/2</sub>, and Ti(III) 2p<sub>1/2</sub> peaks are detected at binding energies of 455.1, 455.6, 456.8, 458.8, 461.3, and 462.3 eV, respectively. After loading the SnO<sub>2</sub> QDs, no Ti(IV) peak is observed, suggesting no oxidation of MXene in the SnO<sub>2</sub> QDs/MXene-52 (Fig. 3f). Meanwhile, the XPS in Sn 3d region has two peaks at 487.2 and 495.6 eV, which are attributed to Sn 3d<sub>5/2</sub> and Sn 3d<sub>3/2</sub> of SnO<sub>2</sub>, confirming the formation of SnO<sub>2</sub> (Fig. S2b). Besides this, the relative intensities of Ti-C, Ti(II), and Ti(III) peaks in SnO<sub>2</sub> QDs/MXene-52 are relatively weaker than pure Ti<sub>3</sub>C<sub>2</sub>T<sub>x</sub>, indicating decreasing Ti<sub>3</sub>C<sub>2</sub>T<sub>x</sub> signal for the hybrid. Furthermore, the slight shift of the Ti-C component to lower binding energy indicates that the synthesis of SnO<sub>2</sub> QDs/MXene hybrid by electrostatic attraction might have caused shift in the electron density (Fig. 3e). All of these observations demonstrate that SnO<sub>2</sub> QDs have been successfully deposited on the surface of the Ti<sub>3</sub>C<sub>2</sub>T<sub>x</sub> sheets. In addition, the introduction of SnO<sub>2</sub> QDs on the Ti<sub>3</sub>C<sub>2</sub>T<sub>x</sub> surface increases the accessible surface area [49], which is evident from the nitrogen adsorption measurements (Fig. S2c). The SnO<sub>2</sub> QDs/MXene-52 shows a typical type I adsorption/desorption

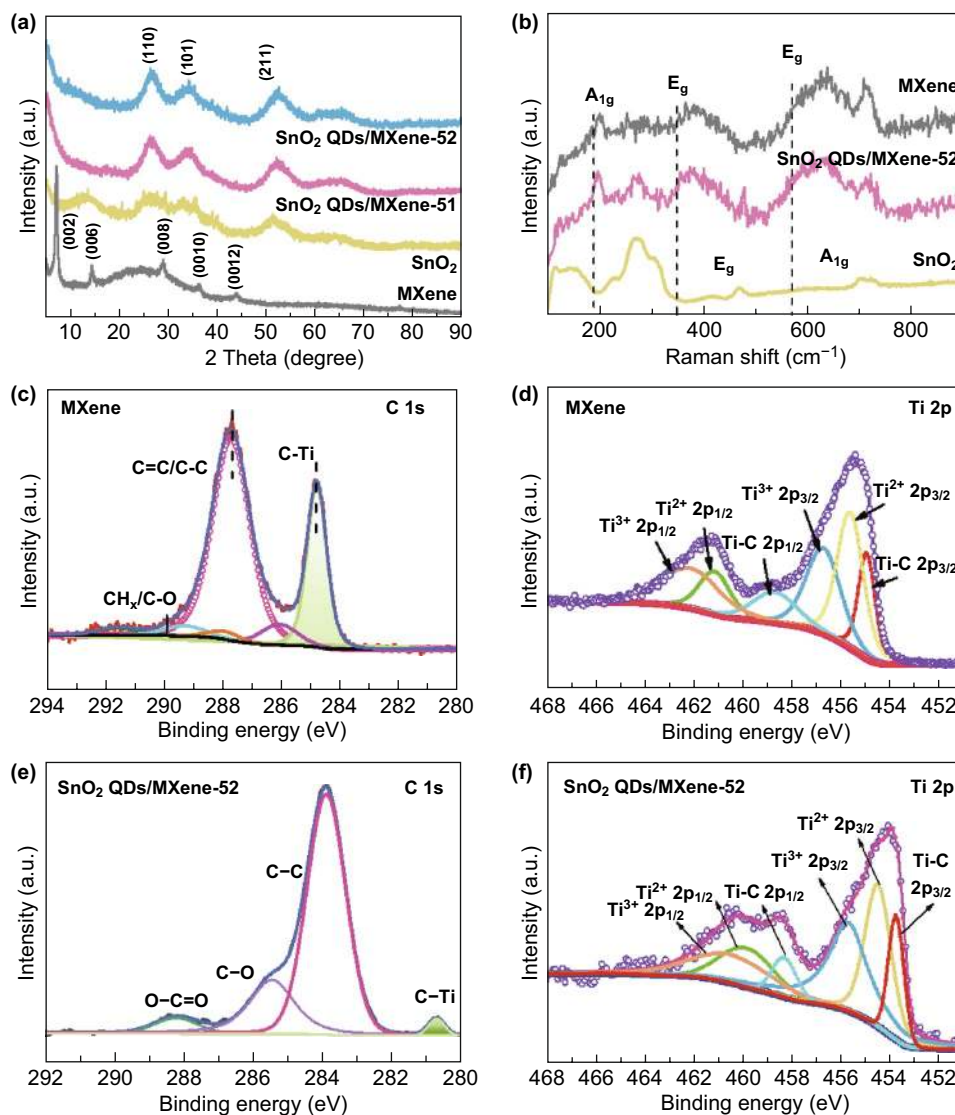


**Fig. 3** **a** XRD patterns, **b** Raman spectra of MXene, SnO<sub>2</sub>, and SnO<sub>2</sub> QDs/MXene hybrid. XPS spectra of **c** MXene for high-resolution C 1s, **d** Ti 2p, **e** SnO<sub>2</sub> QDs/MXene-52 for high-resolution C 1s, **f** Ti 2p

isotherms with a BET specific surface area of 184 m<sup>2</sup> g<sup>-1</sup>, much higher than that of the pure MXene (19 m<sup>2</sup> g<sup>-1</sup>). The large surface area is beneficial for accelerating electrolyte diffusion and accommodating volume change of the SnO<sub>2</sub> QDs during charge/discharge. Thus, much improved lithium storage performances could be expected.

To evaluate the electrochemical performances of the SnO<sub>2</sub> QDs/MXene hybrids as anode materials in LIBs, coin-type half cells were assembled using lithium as counter electrode. CV curves of Ti<sub>3</sub>C<sub>2</sub>T<sub>x</sub> MXene and SnO<sub>2</sub> QDs/MXene hybrids were scanned between 0.01 and 2.5 V. For the pure Ti<sub>3</sub>C<sub>2</sub>T<sub>x</sub> MXene, the broad irreversible reduction peak at

around 0.7 V is observed in the first lithiation process, which is attributed to the formation of a solid electrolyte interphase (SEI) generated from the reaction of Ti<sub>3</sub>C<sub>2</sub>T<sub>x</sub> with Li ion [17]. In the subsequent cycles, the reversible peaks near 0.77 and 1.5 V may be the consequence of the reaction between Li<sup>+</sup> and the titanium-based compounds (Fig. S3a) [50]. For the pure SnO<sub>2</sub> QDs (Fig. S3b), the SnO<sub>2</sub> is considered to transform into Li<sub>x</sub>Sn ( $x \leq 4.4$ ) and Li<sub>2</sub>O during the initial discharge process (lithium insertion). The cathodic peak at 0.05 V result from the alloying process of Sn to Li<sub>x</sub>Sn ( $0 \leq x \leq 4.4$ ), and the strong anode peak at about 0.5 V is caused by the de-alloying process of Li<sub>x</sub>Sn ( $0 \leq x \leq 4.4$ ).

The anode peak at 1.2 V is caused by the partial reversible transformation of Sn to SnO<sub>2</sub> owing to its quantum size [51, 52]. However, in the second and third cycles of the pure SnO<sub>2</sub>, the intensities of the cathodic and anodic peaks show continuous and significant decline, indicating rapid capacity degradation because of the structural variation of SnO<sub>2</sub> during lithiation/delithiation processes (Fig. S3b). The SnO<sub>2</sub> QDs/MXene-52 (Fig. 4a) shows CV curves with similar characteristic peaks, but the curves in the 2nd and 3rd cycles almost overlap, indicating good cycle performance. In comparison with the SnO<sub>2</sub> QDs/MXene-51 (Fig. 4b), the SnO<sub>2</sub> QDs/MXene-52 display better overlapping CV curves with the same peak positions, implying excellent reversibility in its conversion reaction.

Furthermore, the GCD profiles (Fig. 4c, d) of the SnO<sub>2</sub> QDs/MXene at 50 mA g<sup>-1</sup> coincides well with the CV curves. The GCD profile of the Ti<sub>3</sub>C<sub>2</sub>T<sub>x</sub> and SnO<sub>2</sub> QDs electrodes were also tested at the same conditions (Fig. S3c, d). In the initial discharge profile of the SnO<sub>2</sub> QDs/MXene hybrids, the plateaus at 0.7 and 0.05 V correspond to the

SEI formation and lithium alloying; while during the initial charge, the plateaus at 0.5 and 1.2 V relate to lithium de-alloying and partial reversible SnO<sub>2</sub> formation, respectively. The reversible capacity of the SnO<sub>2</sub> QDs/MXene-52 is 887.4 mAh g<sup>-1</sup> in the first cycle, with initial Coulombic efficiency (CE) of about 51.2%. The low CE might have resulted from the SEI and Li<sub>2</sub>O formation as well as the electrolyte decomposition. In the 5th cycle, the capacity was determined to be about 847.6 mAh g<sup>-1</sup> and the corresponding CE reached about 100%. With the SEI film protection, the capacity reaches a stable state. In contrast, the SnO<sub>2</sub> QDs/MXene-51 delivers an initial reversible capacity of 897.5 mAh g<sup>-1</sup> with a CE of 43.0% (Fig. 4d). The results indicate that the introduction of more SnO<sub>2</sub> QDs can increase available active sites and the capacity of the hybrid material, but at the same time cause more side reactions and reduce the initial CE, due to its ultra-small particle size and high surface area. Therefore, only appropriate ratio of SnO<sub>2</sub> QDs and MXene sheets could reach an optimum electrochemical performance.

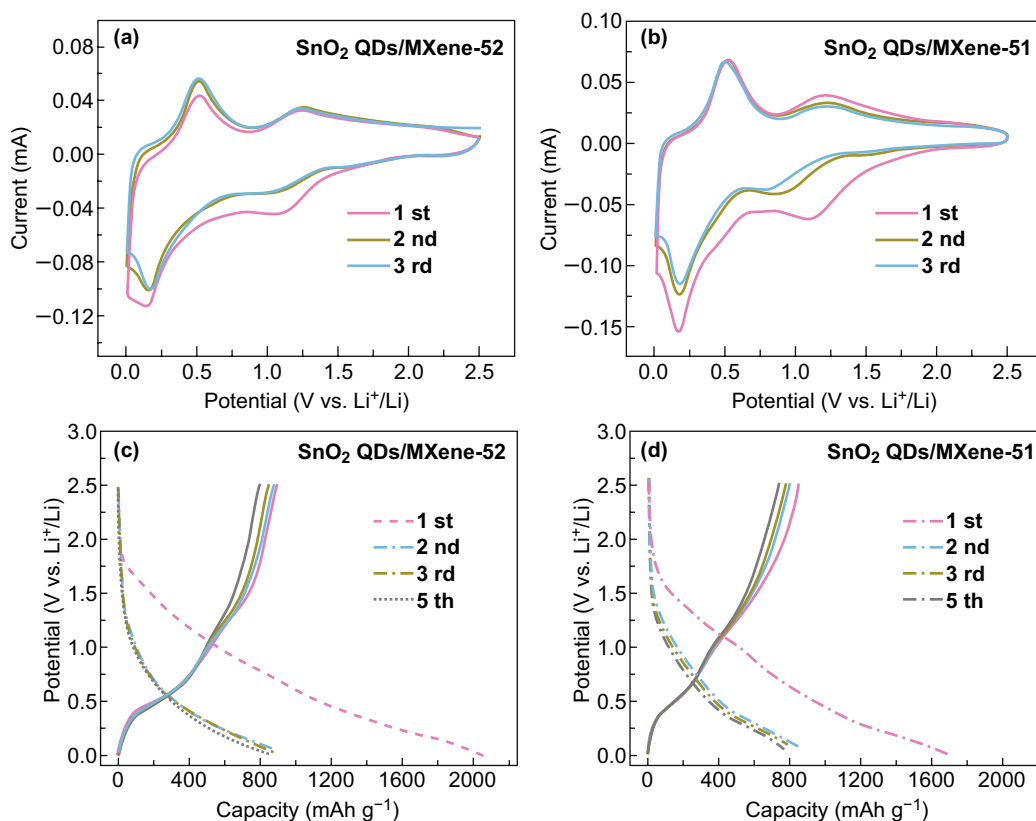


**Fig. 4** Electrochemical performances as anode in LIBs. **a, b** CV curves of SnO<sub>2</sub> QDs/MXene at a scan rate of 0.1 mV s<sup>-1</sup> in 0.01–2.5 V. **c, d** Charge/discharge curves of SnO<sub>2</sub> QDs/MXene at 50 mA g<sup>-1</sup>

Figure 5a shows the comparison of the charge/discharge cycle performance among  $\text{Ti}_3\text{C}_2\text{T}_x$  MXene,  $\text{SnO}_2$  QDs, and  $\text{SnO}_2$  QDs/MXene at  $100 \text{ mA g}^{-1}$ . The bare  $\text{Ti}_3\text{C}_2\text{T}_x$  MXene has a low initial capacity of  $79.2 \text{ mAh g}^{-1}$  with a CE of 34.2%, which is attributed to the restacking of MXene nanosheets [36]. The initial capacity of the pure  $\text{SnO}_2$  QDs can reach  $835.9 \text{ mAh g}^{-1}$ , but it fades very rapidly due to the severe pulverization of  $\text{SnO}_2$  during charge/discharge. After 20 cycles, the capacity remains only  $144.6 \text{ mAh g}^{-1}$  with a capacity retention ratio of about 17% of the initial capacity. In contrast, by electrostatic self-assembly of the  $\text{SnO}_2$  QDs on the 2D  $\text{Ti}_3\text{C}_2\text{T}_x$  MXene nanosheets, the  $\text{SnO}_2$  QDs/

MXene hybrids exhibit much enhanced cycle stability. The capacity of  $\text{SnO}_2$  QDs/MXene-52 reaches to  $659.8 \text{ mAh g}^{-1}$  with 91% retention of the initial capacity after 100 cycles, which is much higher than that of the pure  $\text{SnO}_2$  QDs and  $\text{Ti}_3\text{C}_2\text{T}_x$  MXene. In a comparative evaluation of  $\text{SnO}_2$  QDs/MXene hybrids with different  $\text{SnO}_2$ /MXene ratio, it is found that the  $\text{SnO}_2$  QDs/MXene-52 with abundant MXene shows better cycle stability than the  $\text{SnO}_2$  QDs/MXene-51, indicating the importance of adequate MXene substrate in achieving optimum performance [53].

Another attractive feature of the  $\text{SnO}_2$  QDs/MXene electrodes is the excellent rate performance. As shown in Fig. 5b,

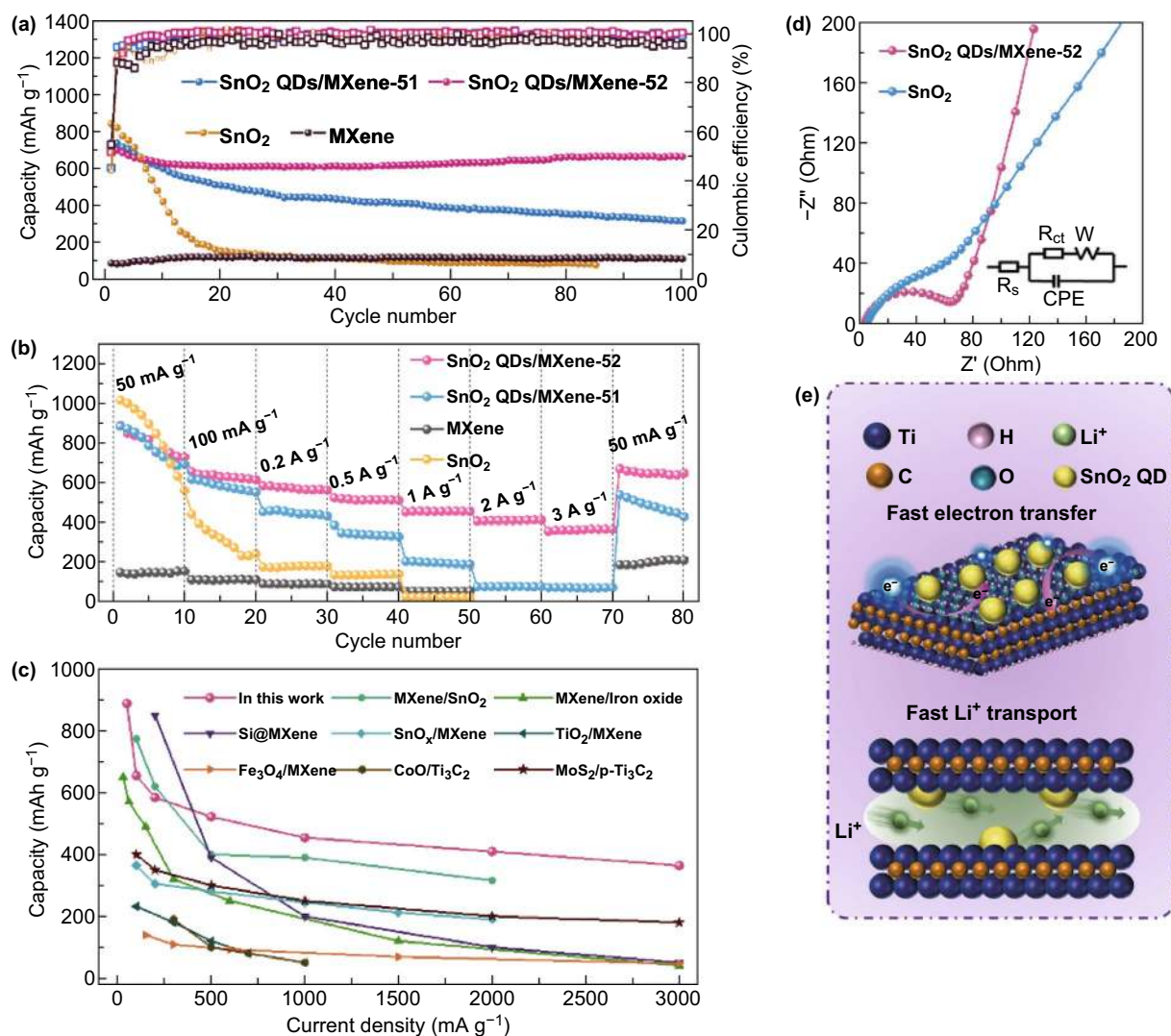


**Fig. 5** **a** Cycle stability, **b** rate performance of all the samples as LIB electrodes. **c** Comparison of rate capacity between the  $\text{SnO}_2$  QDs/MXene-52 and other MXene-based electrode materials reported for LIBs. **d** Nyquist plots of the  $\text{SnO}_2$  QDs/MXene-52 and the pure  $\text{SnO}_2$  electrodes; **e** energy storage mechanism of the 0D–2D  $\text{SnO}_2$  QDs/MXene hybrids



the SnO<sub>2</sub> QDs/MXene electrode exhibit much enhanced rate capability compared to pure SnO<sub>2</sub> QDs. Especially for SnO<sub>2</sub> QDs/MXene-52, as the current density increases from 50 to 100, 200, 500, 1000, 2000, and 3000 mA g<sup>-1</sup>, its reversible capacity remains 887.4, 655.2, 584.5, 522.0, 454.7, 409.7, and 364.0 mAh g<sup>-1</sup>, respectively, demonstrating superior rate performance. When the current density returns back to 50 mA g<sup>-1</sup> again, the capacity recovers to 688.1 mAh g<sup>-1</sup>. These results indicate that the unique 0D–2D architecture of the SnO<sub>2</sub> QDs/MXene hybrids facilitates the Li ion diffusion and the electron transfer, thereby enhancing the reaction kinetics and the rate capability. The comparison of the rate performance for QDs/MXene-52 with previously reported SnO<sub>2</sub>-based anodes and other MXene-based anodes is plotted in Fig. 5c. The SnO<sub>2</sub> QDs/MXene-52 demonstrate superior rate capability compared to other anode materials based on MXene matrix, such as SnO<sub>2</sub> QDs/MXene backbone [40], SnO<sub>x</sub> nanosheets/MXene [54], Fe<sub>2</sub>O<sub>3</sub>/MXene [37], Fe<sub>3</sub>O<sub>4</sub> nanoparticles@MXene [50], TiO<sub>2</sub> nanowire/Ti<sub>3</sub>C<sub>2</sub> [55], CoO nanoparticles/Ti<sub>3</sub>C<sub>2</sub> [44], MoS<sub>2</sub>/p-Ti<sub>3</sub>C<sub>2</sub> [56], and Si@Ti<sub>3</sub>C<sub>2</sub> [57] etc.

Electrochemical impedance spectroscopy was employed to compare the reaction kinetics of the SnO<sub>2</sub> QDs/MXene-52 and the bare SnO<sub>2</sub> QDs. The typical Nyquist plots of the two electrodes (Fig. 5d) consist of a compressed semicircle in the intermediate frequency region and a diagonal line in the low frequency range. The semicircle is related to the charge transfer resistance ( $R_{ct}$ ), and the oblique line is related to Warburg impedance, suggesting the diffusion of Li ion in the active materials [58]. The  $R_{ct}$  values of the SnO<sub>2</sub> QDs/MXene-52 and SnO<sub>2</sub> QDs electrode were calculated to be 75.50 and 100.20 Ω, respectively. Obviously, SnO<sub>2</sub> QDs/MXene-52 possesses much lower  $R_{ct}$  value compared to bare SnO<sub>2</sub> QDs. This can be attributed to the high electrical conductivity of the MXene and the fast charge diffusion reaction due to its unique 0D–2D structure. Moreover, the SnO<sub>2</sub> QDs/MXene-52 shows a relatively steep low-frequency tail, indicative of high Li ion diffusibility, which results from the efficient ion transfer pathways constructed by MXene.

The above excellent electrochemical performances are because of the synergic effect between MXene nanosheets and SnO<sub>2</sub> QDs, and the mechanism is illustrated in Fig. 5e. In the SnO<sub>2</sub> QDs/MXene hybrids, the MXene nanosheets act as 2D substrates for uniform anchoring of SnO<sub>2</sub> QDs. The MXene nanosheets prevent the aggregation of SnO<sub>2</sub>

QDs and work as an elastic buffer space to adapt to the volume expansion/contraction of SnO<sub>2</sub> QDs during charging and discharging, thus leading to good cycle stability. Furthermore, MXene nanosheets with good electric conductivity construct effective conductive channels for SnO<sub>2</sub> QDs, facilitating fast charge transport and improving the rate performance. Moreover, the unique 0D–2D structure offers massive electrochemically active sites for high specific capacity, which contribute in improving the electrochemical performance of electrode materials, thus excellent lithium-ion storage performances are obtained for SnO<sub>2</sub> QDs/MXene hybrids.

## 4 Conclusions

The 0D–2D SnO<sub>2</sub> QDs/MXene hybrids have been successfully synthesized by an efficient electrostatic self-assembly strategy. The 0D SnO<sub>2</sub> QDs with an average size of 4.7 nm are uniformly distributed on the 2D MXene nanosheets with strong adhesion, acting as structurally stable host for lithium storage. The 2D MXene nanosheets buffer the volume change of SnO<sub>2</sub> QDs during charge/discharge and construct effective channels for charge transport. Besides this, the 0D–2D structure creates additional active sites. The 2D conductive Ti<sub>3</sub>C<sub>2</sub>T<sub>x</sub> MXene, ultra-small SnO<sub>2</sub> QDs, and unique 0D–2D nano-architecture are synergistically responsible for the outstanding electrochemical performances of the SnO<sub>2</sub> QDs/MXene hybrids. As an anode for LIBs, it exhibits a high specific capacity of 887.4 mAh g<sup>-1</sup> at 50 mA g<sup>-1</sup>, excellent rate capability (364 mAh g<sup>-1</sup> at 3 A g<sup>-1</sup>), and superior cycle stability (659.8 mAh g<sup>-1</sup> after 100 cycles with 91% retention). These results indicate that the 0D–2D SnO<sub>2</sub> QDs/MXene is a promising anode material for advanced LIBs. In addition, the electrostatic self-assembly method could be extended to other transition metal oxide/MXene hybrids and will have potential applications in sodium-ion batteries, potassium-ion batteries, and supercapacitors.

**Acknowledgements** This work was supported by the National Key Research and Development Program of China “New Energy Project for Electric Vehicle” (2016YFB0100204), the National Natural Science Foundation of China (Nos. 51772030, 21805011, 51572011, 51802012), the Joint Funds of the National Natural Science Foundation of China (U1564206) and Beijing Key Research

and Development Plan (Z181100004518001) and China Postdoctoral Science Foundation (Nos. 2017M620637, 2018M643697, 2019T120930).

**Open Access** This article is distributed under the terms of the Creative Commons Attribution 4.0 International License (<http://creativecommons.org/licenses/by/4.0/>), which permits unrestricted use, distribution, and reproduction in any medium, provided you give appropriate credit to the original author(s) and the source, provide a link to the Creative Commons license, and indicate if changes were made.

**Electronic supplementary material** The online version of this article (<https://doi.org/10.1007/s40820-019-0296-7>) contains supplementary material, which is available to authorized users.

## References

- M. Li, J. Lu, Z. Chen, K. Amine, 30 years of lithium-ion batteries. *Adv. Mater.* **30**(33), 1800561 (2018). <https://doi.org/10.1002/adma.201800561>
- X. Zuo, J. Zhu, P. Müller-Buschbaum, Y.-J. Cheng, Silicon based lithium-ion battery anodes: a chronicle perspective review. *Nano Energy* **31**, 113–143 (2017). <https://doi.org/10.1016/j.nanoen.2016.11.013>
- H. Liu, M. Jia, Q. Zhu, B. Cao, R. Chen, Y. Wang, F. Wu, B. Xu, 3D–0D graphene-Fe<sub>3</sub>O<sub>4</sub> quantum dot hybrids as high-performance anode materials for sodium-ion batteries. *ACS Appl. Mater. Interfaces* **8**(40), 26878–26885 (2016). <https://doi.org/10.1021/acsami.6b09496>
- Y. Zhao, X. Li, B. Yan, D. Xiong, D. Li, S. Lawes, X. Sun, Recent developments and understanding of novel mixed transition-metal oxides as anodes in lithium ion batteries. *Adv. Energy Mater.* **6**(8), 1502175 (2016). <https://doi.org/10.1002/aenm.201502175>
- P. Lian, J. Wang, D. Cai, G. Liu, Y. Wang, H. Wang, Design and synthesis of porous nano-sized Sn@C/graphene electrode material with 3D carbon network for high-performance lithium-ion batteries. *J. Alloys Compd.* **604**, 188–195 (2014). <https://doi.org/10.1016/j.jallcom.2014.03.116>
- J. Mao, T. Zhou, Y. Zheng, H. Gao, H.K. Liu, Z. Guo, Two-dimensional nanostructures for sodium-ion battery anodes. *J. Mater. Chem. A* **6**(8), 3284–3303 (2018). <https://doi.org/10.1039/c7ta10500b>
- L. Fei, Y. Jiang, Y. Xu, G. Chen, Y. Li, X. Xu, S. Deng, H. Luo, A novel solvent-free thermal reaction of ferrocene and sulfur for one-step synthesis of iron sulfide and carbon nanocomposites and their electrochemical performance. *J. Power Sources* **265**, 1–5 (2014). <https://doi.org/10.1016/j.jpowsour.2014.04.110>
- T. Zhou, W.K. Pang, C. Zhang, J. Yang, Z. Chen, H.K. Liu, Z. Guo, Enhanced sodium-ion battery performance by structural phase transition from two-dimensional hexagonal-SnS<sub>2</sub> to orthorhombic-SnS. *ACS Nano* **8**(8), 8323–8333 (2014). <https://doi.org/10.1021/nn503582c>
- S.L. Zhang, B.Y. Guan, H.B. Wu, X.W.D. Lou, Metal-organic framework-assisted synthesis of compact Fe<sub>2</sub>O<sub>3</sub> nanotubes in Co<sub>3</sub>O<sub>4</sub> host with enhanced lithium storage properties. *Nano Micro Lett.* **10**(3), 44 (2018). <https://doi.org/10.1007/s40820-018-0197-1>
- A. Bai, L. Wang, J. Li, X. He, J. Wang, J. Wang, Composite of graphite/phosphorus as anode for lithium-ion batteries. *J. Power Sources* **289**, 100–104 (2015). <https://doi.org/10.1016/j.jpowsour.2015.04.168>
- X. Yu, H.J. Kim, J.-Y. Hong, Y.M. Jung, K.D. Kwon, J. Kong, H.S. Park, Elucidating surface redox charge storage of phosphorus-incorporated graphenes with hierarchical architectures. *Nano Energy* **15**, 576–586 (2015). <https://doi.org/10.1016/j.nanoen.2015.05.010>
- W. Zhang, W.K. Pang, V. Sencadas, Z. Guo, Understanding high-energy-density Sn<sub>4</sub>P<sub>3</sub> anodes for potassium-ion batteries. *Joule* **2**(8), 1534–1547 (2018). <https://doi.org/10.1016/j.joule.2018.04.022>
- L. Pan, Y. Zhang, F. Lu, Y. Du, Z. Lu et al., Exposed facet engineering design of graphene-SnO<sub>2</sub> nanorods for ultrastable Li-ion batteries. *Energy Storage Mater.* (2018). <https://doi.org/10.1016/j.ensm.2018.10.007>
- H. Wang, X. Jiang, Y. Chai, X. Yang, R. Yuan, Sandwich-like C@SnO<sub>2</sub>/Sn/void@C hollow spheres as improved anode materials for lithium ion batteries. *J. Power Sources* **379**, 191–196 (2018). <https://doi.org/10.1016/j.jpowsour.2018.01.054>
- B. Zhao, Z. Wang, S. Wang, J. Jiang, J. Si, S. Huang, Z. Chen, W. Li, Y. Jiang, Sandwiched spherical tin dioxide/graphene with a three-dimensional interconnected closed pore structure for lithium storage. *Nanoscale* **10**(34), 16116–16126 (2018). <https://doi.org/10.1039/c8nr03776k>
- P. Deng, J. Yang, S. Li, T.-E. Fan, H.-H. Wu et al., High initial reversible capacity and long life of ternary SnO<sub>2</sub>-Co-carbon nanocomposite anodes for lithium-ion batteries. *Nano Micro Lett.* **11**, 18 (2019). <https://doi.org/10.1007/s40820-019-0246-4>
- J. Liang, C. Yuan, H. Li, K. Fan, Z. Wei, H. Sun, J. Ma, Growth of SnO<sub>2</sub> nanoflowers on N-doped carbon nanofibers as anode for Li- and Na-ion batteries. *Nano Micro Lett.* **10**(2), 21 (2018). <https://doi.org/10.1007/s40820-017-0172-2>
- H. Li, Q. Su, J. Kang, M. Huang, M. Feng, H. Feng, P. Huang, G. Du, Porous SnO<sub>2</sub> hollow microspheres as anodes for high-performance lithium ion battery. *Mater. Lett.* **217**, 276–280 (2018). <https://doi.org/10.1016/j.matlet.2018.01.015>
- Y.T. Liu, P. Zhang, N. Sun, B. Anasori, Q.Z. Zhu, H. Liu, Y. Gogotsi, B. Xu, Self-assembly of transition metal oxide nanostructures on MXene nanosheets for fast and stable lithium storage. *Adv. Mater.* **30**(23), 1707334 (2018). <https://doi.org/10.1002/adma.201707334>
- S. Abouali, M. Akbari Garakani, J.-K. Kim, Ultrafine SnO<sub>2</sub> nanoparticles encapsulated in ordered mesoporous carbon framework for Li-ion battery anodes. *Electrochim. Acta* **284**, 436–443 (2018). <https://doi.org/10.1016/j.electacta.2018.07.162>

21. N. Hu, X. Lv, Y. Dai, L. Fan, D. Xiong, X. Li, SnO<sub>2</sub>/reduced graphene oxide interlayer mitigating the shuttle effect of Li-S batteries. *ACS Appl. Mater. Interfaces* **10**(22), 18665–18674 (2018). <https://doi.org/10.1021/acsami.8b03255>
22. J. Abe, K. Takahashi, K. Kawase, Y. Kobayashi, S. Shiratori, Self-standing carbon nanofiber and SnO<sub>2</sub> nanorod composite as a high-capacity and high-rate-capability anode for lithium-ion batteries. *ACS Appl. Nano Mater.* **1**(6), 2982–2989 (2018). <https://doi.org/10.1021/acsnm.8b00586>
23. D. Ma, Y. Li, H. Mi, S. Luo, P. Zhang, Z. Lin, J. Li, H. Zhang, Robust SnO<sub>2-x</sub> nanoparticle-impregnated carbon nanofibers with outstanding electrochemical performance for advanced sodium-ion batteries. *Angew. Chem. Int. Ed.* **57**(29), 8901–8905 (2018). <https://doi.org/10.1002/anie.201802672>
24. R. Jia, J. Yue, Q. Xia, J. Xu, X. Zhu, S. Sun, T. Zhai, H. Xia, Carbon shelled porous SnO<sub>2-δ</sub> nanosheet arrays as advanced anodes for lithium-ion batteries. *Energy Storage Mater.* **13**, 303–311 (2018). <https://doi.org/10.1016/j.ensm.2018.02.009>
25. Y. Cheng, J. Huang, H. Qi, L. Cao, J. Yang, Q. Xi, X. Luo, K. Yanagisawa, J. Li, Adjusting the chemical bonding of SnO<sub>2</sub>@CNT composite for enhanced conversion reaction kinetics. *Small* **13**(31), 1700656 (2017). <https://doi.org/10.1002/sml.201700656>
26. Y. Cheng, J. Huang, H. Qi, L. Cao, X. Luo, J. Li, Z. Xu, J. Yang, Controlling the Sn-C bonds content in SnO<sub>2</sub>@CNTs composite to form in situ pulverized structure for enhanced electrochemical kinetics. *Nanoscale* **9**(47), 18681–18689 (2017). <https://doi.org/10.1039/c7nr05556k>
27. P. Simon, Two-dimensional MXene with controlled interlayer spacing for electrochemical energy storage. *ACS Nano* **11**(3), 2393–2396 (2017). <https://doi.org/10.1021/acsnano.7b01108>
28. L. Yu, L. Hu, B. Anasori, Y.-T. Liu, Q. Zhu, P. Zhang, Y. Gogotsi, B. Xu, MXene-bonded activated carbon as a flexible electrode for high-performance supercapacitors. *ACS Energy Lett.* **3**(7), 1597–1603 (2018). <https://doi.org/10.1021/acsenerylett.8b00718>
29. C.J. Zhang, S.J. Kim, M. Ghidui, M.-Q. Zhao, M.W. Barsoum, V. Nicolosi, Y. Gogotsi, Layered orthorhombic Nb<sub>2</sub>O<sub>5</sub>@Nb<sub>4</sub>C<sub>3</sub>T<sub>x</sub> and TiO<sub>2</sub>@Ti<sub>3</sub>C<sub>2</sub>T<sub>x</sub> hierarchical composites for high performance Li-ion batteries. *Adv. Funct. Mater.* **26**(23), 4143–4151 (2016). <https://doi.org/10.1002/adfm.201600682>
30. C. Zhang, M. Beidaghi, M. Naguib, M.R. Lukatskaya, M.-Q. Zhao et al., Synthesis and charge storage properties of hierarchical niobium pentoxide/carbon/niobium carbide (MXene) hybrid materials. *Chem. Mater.* **28**(11), 3937–3943 (2016). <https://doi.org/10.1021/acs.chemmater.6b01244>
31. C.J. Zhang, S. Pinilla, N. McEvoy, C.P. Cullen, B. Anasori et al., Oxidation stability of colloidal two-dimensional titanium carbides (MXenes). *Chem. Mater.* **29**(11), 4848–4856 (2017). <https://doi.org/10.1021/acs.chemmater.7b00745>
32. M.Q. Zhao, C.E. Ren, Z. Ling, M.R. Lukatskaya, C. Zhang et al., Flexible MXene/carbon nanotube composite paper with high volumetric capacitance. *Adv. Mater.* **27**(2), 339–345 (2015). <https://doi.org/10.1002/adma.201404140>
33. X. Xie, S. Wang, K. Kretschmer, G. Wang, Two-dimensional layered compound based anode materials for lithium-ion batteries and sodium-ion batteries. *J. Colloid Interface Sci.* **499**, 17–32 (2017). <https://doi.org/10.1016/j.jcis.2017.03.077>
34. X. Xie, M.-Q. Zhao, B. Anasori, K. Maleski, C.E. Ren et al., Porous heterostructured MXene/carbon nanotube composite paper with high volumetric capacity for sodium-based energy storage devices. *Nano Energy* **26**, 513–523 (2016). <https://doi.org/10.1016/j.nanoen.2016.06.005>
35. C.J. Zhang, S.H. Park, A. Seral-Ascaso, S. Barwich, N. McEvoy et al., High capacity silicon anodes enabled by MXene viscous aqueous ink. *Nat. Commun.* **10**(1), 849 (2019). <https://doi.org/10.1038/s41467-019-08383-y>
36. G. Zou, Z. Zhang, J. Guo, B. Liu, Q. Zhang, C. Fernandez, Q. Peng, Synthesis of MXene/Ag composites for extraordinary long cycle lifetime lithium storage at high rates. *ACS Appl. Mater. Interfaces* **8**(34), 22280–22286 (2016). <https://doi.org/10.1021/acsami.6b08089>
37. A. Ali, K. Hantanasirisakul, A. Abdala, P. Urbankowski, M.Q. Zhao, B. Anasori, Y. Gogotsi, B. Aissa, K.A. Mahmoud, Effect of synthesis on performance of MXene/iron oxide anode material for lithium-ion batteries. *Langmuir* **34**(38), 11325–11334 (2018). <https://doi.org/10.1021/acs.langmuir.8b01953>
38. M.-Q. Zhao, M. Torelli, C.E. Ren, M. Ghidui, Z. Ling, B. Anasori, M.W. Barsoum, Y. Gogotsi, 2D titanium carbide and transition metal oxides hybrid electrodes for Li-ion storage. *Nano Energy* **30**, 603–613 (2016). <https://doi.org/10.1016/j.nanoen.2016.10.062>
39. C. Chen, X. Xie, B. Anasori, A. Sarycheva, T. Makaryan et al., MoS<sub>2</sub>-on-MXene heterostructures as highly reversible anode materials for lithium-ion batteries. *Angew. Chem. Int. Ed.* **57**(7), 1846–1850 (2018). <https://doi.org/10.1002/anie.201710616>
40. J. Xiong, L. Pan, H. Wang, F. Du, Y. Chen, J. Yang, C. Zhang, Synergistically enhanced lithium storage performance based on titanium carbide nanosheets (MXene) backbone and SnO<sub>2</sub> quantum dots. *Electrochim. Acta* **268**, 503–511 (2018). <https://doi.org/10.1016/j.electacta.2018.02.090>
41. M. Boota, B. Anasori, C. Voigt, M.Q. Zhao, M.W. Barsoum, Y. Gogotsi, Pseudocapacitive electrodes produced by oxidant-free polymerization of pyrrole between the layers of 2D titanium carbide (MXene). *Adv. Mater.* **28**(7), 1517–1522 (2016). <https://doi.org/10.1002/adma.201504705>
42. X. Lu, H. Wang, Z. Wang, Y. Jiang, D. Cao, G. Yang, Room-temperature synthesis of colloidal SnO<sub>2</sub> quantum dot solution and ex situ deposition on carbon nanotubes as anode materials for lithium ion batteries. *J. Alloys Compd.* **680**, 109–115 (2016). <https://doi.org/10.1016/j.jallcom.2016.04.128>
43. J. Yan, C.E. Ren, K. Maleski, C.B. Hatter, B. Anasori, P. Urbankowski, A. Sarycheva, Y. Gogotsi, Flexible MXene/graphene films for ultrafast supercapacitors with outstanding volumetric capacitance. *Adv. Funct. Mater.* **27**(30), 1701264 (2017). <https://doi.org/10.1002/adfm.201701264>
44. X. Li, J. Zhu, Y. Fang, W. Lv, F. Wang, Y. Liu, H. Liu, Hydrothermal preparation of CoO/Ti<sub>3</sub>C<sub>2</sub> composite material for lithium-ion batteries with enhanced electrochemical performance. *J. Electroanal. Chem.* **817**, 1–8 (2018). <https://doi.org/10.1016/j.jelechem.2018.03.031>



45. H. Zhang, P. Zhang, W. Zheng, W. Tian, J. Chen, Y. Zhang, Z. Sun, 3D d-Ti<sub>3</sub>C<sub>2</sub> xerogel framework decorated with core-shell SnO<sub>2</sub>@C for high-performance lithium-ion batteries. *Electrochim. Acta* **285**, 94–102 (2018). <https://doi.org/10.1016/j.electacta.2018.07.198>
46. M. Sahoo, S. Ramaprabhu, One-pot environment-friendly synthesis of boron doped graphene-SnO<sub>2</sub> for anodic performance in Li ion battery. *Carbon* **127**, 627–635 (2018). <https://doi.org/10.1016/j.carbon.2017.11.056>
47. Z. Ma, X. Zhou, W. Deng, D. Lei, Z. Liu, 3D porous MXene (Ti<sub>3</sub>C<sub>2</sub>)/reduced graphene oxide hybrid films for advanced lithium storage. *ACS Appl. Mater. Interfaces* **10**(4), 3634–3643 (2018). <https://doi.org/10.1021/acsami.7b17386>
48. W. Bao, X. Xie, J. Xu, X. Guo, J. Song, W. Wu, D. Su, G. Wang, Confined sulfur in 3D MXene/reduced graphene oxide hybrid nanosheets for lithium-sulfur battery. *Chemistry* **23**(51), 12613–12619 (2017). <https://doi.org/10.1002/chem.201702387>
49. J. Zhu, Y. Tang, C. Yang, F. Wang, M. Cao, Composites of TiO<sub>2</sub> nanoparticles deposited on Ti<sub>3</sub>C<sub>2</sub> MXene nanosheets with enhanced electrochemical performance. *J. Electrochem. Soc.* **163**(5), A785–A791 (2016). <https://doi.org/10.1149/2.0981605jes>
50. Y. Wang, Y. Li, Z. Qiu, X. Wu, P. Zhou et al., Fe<sub>3</sub>O<sub>4</sub>@Ti<sub>3</sub>C<sub>2</sub> MXene hybrids with ultrahigh volumetric capacity as an anode material for lithium-ion batteries. *J. Mater. Chem. A* **6**(24), 11189–11197 (2018). <https://doi.org/10.1039/c8ta00122g>
51. X. Ao, J. Jiang, Y. Ruan, Z. Li, Y. Zhang, J. Sun, C. Wang, Honeycomb-inspired design of ultrafine SnO<sub>2</sub>@C nanospheres embedded in carbon film as anode materials for high performance lithium- and sodium-ion battery. *J. Power Sources* **359**, 340–348 (2017). <https://doi.org/10.1016/j.jpowsour.2017.05.064>
52. D. Cui, Z. Zheng, X. Peng, T. Li, T. Sun, L. Yuan, Fluorine-doped SnO<sub>2</sub> nanoparticles anchored on reduced graphene oxide as a high-performance lithium ion battery anode. *J. Power Sources* **362**, 20–26 (2017). <https://doi.org/10.1016/j.jpowsour.2017.07.024>
53. X. Wang, X. Zhou, K. Yao, J. Zhang, Z. Liu, A SnO<sub>2</sub>/graphene composite as a high stability electrode for lithium ion batteries. *Carbon* **49**(1), 133–139 (2011). <https://doi.org/10.1016/j.carbon.2010.08.052>
54. X. Sun, Y. Liu, J. Zhang, L. Hou, J. Sun, C. Yuan, Facile construction of ultrathin SnO<sub>2</sub> nanosheets decorated MXene (Ti<sub>3</sub>C<sub>2</sub>) nanocomposite towards Li-ion batteries as high performance anode materials. *Electrochim. Acta* **295**, 237–245 (2019). <https://doi.org/10.1016/j.electacta.2018.10.152>
55. W. Lv, J. Zhu, F. Wang, Y. Fang, Facile synthesis and electrochemical performance of TiO<sub>2</sub> nanowires/Ti<sub>3</sub>C<sub>2</sub> composite. *J. Mater. Sci.* **29**(6), 4881–4887 (2018). <https://doi.org/10.1007/s10854-017-8446-5>
56. M. Zheng, R. Guo, Z. Liu, B. Wang, L. Meng, F. Li, T. Li, Y. Luo, MoS<sub>2</sub> intercalated *p*-Ti<sub>3</sub>C<sub>2</sub> anode materials with sandwich-like three dimensional conductive networks for lithium-ion batteries. *J. Alloys Compd.* **735**, 1262–1270 (2018). <https://doi.org/10.1016/j.jallcom.2017.11.250>
57. F. Kong, X. He, Q. Liu, X. Qi, D. Sun, Y. Zheng, R. Wang, Y. Bai, Enhanced reversible Li-ion storage in Si@Ti<sub>3</sub>C<sub>2</sub> MXene nanocomposite. *Electrochem. Commun.* **97**, 16–21 (2018). <https://doi.org/10.1016/j.elecom.2018.10.003>
58. B. Cao, Q. Zhang, H. Liu, B. Xu, S. Zhang et al., Graphitic carbon nanocage as a stable and high power anode for potassium-ion batteries. *Adv. Energy Mater.* **8**(25), 1801149 (2018). <https://doi.org/10.1002/aenm.201801149>